Ultrasoft hydrogel semiconductor

Yahao Dai[1], Shinya Wai[1], Pengju Li[3], Zhiqiang Cao[2], Yang Li[1], Naisong Shan[1], Yunfei Wang[2,4], Youdi Liu[1], Wei Liu[1], Songsong Li[1], Nan Li[1], Shivani Chatterji[1], Yuzi Liu[5], Sean Lee[3], Chris Fry[5], Cheng Zhang[1], Max Weires[1], Sean Sutyak[1], Jiuyun Shi[3], Chenhui Zhu[4], Jie Xu[5], Bozhi Tian[3], Xiaodan Gu[2], Sihong Wang[1,5,*]

[1] Pritzker School of Molecular Engineering, The University of Chicago, Chicago, IL, USA.

[2] School of Polymer Science and Engineering, Center for Optoelectronic Materials and Devices, The University of Southern Mississippi, Hattiesburg, MS, USA.

[3] Department of Chemistry, The University of Chicago, Chicago, IL, USA.

[4] Advanced Light Source, Lawrence Berkeley National Laboratory, Berkeley, CA, USA.

[5] Nanoscience and Technology Division and Center for Molecular Engineering, Argonne National Laboratory, Lemont, IL, USA.

* e-mail: sihongwang@uchicago.edu

Abstract

Hydrogels provide the best mechanical and chemical similarities with biological tissues and, thereby, have been widely used in biotechnologies[1–4]. Semiconductors offer a variety of advanced electronic and optoelectronic functions[5], including signal amplification, sensing, photo-stimulation, catalysis, etc. For bioelectronic applications of semiconductors, the embodiment of semiconducting properties onto hydrogel designs can greatly improve not only the biointerface intimacy but also bio-interactive functions. However, this remains formidable due to the low hydrophilicity of semiconducting polymers. Here, we report a solvent-affinity-induced assembly method that allows the use of water-insoluble semiconducting polymers to build double-network hydrogels. The resulting hydrogel semiconductor simultaneously achieves a tissue-level modulus of 81 kPa and stretchability of 150% strain, while maintaining efficient charge transport pathways with high mobility of 1.4 $cm^2 V^{-1} s^{-1}$. When the hydrogel semiconductor interfaces with bio-tissues, we show that the tissue-level modulus enables highly conformable attachment and suppressed immune reaction. Moreover, the high-porosity nature of hydrogel enhances the molecular interactions at semiconductor-biofluid interfaces, leading to volumetric biosensing with higher sensitivity and photo-modulation with higher response. These results indicate that hydrogel semiconductors could serve as the ideal functional biointerfaces offering multi-modal sensing and

modulation functions, the best biocompatibility, and maximized biomolecular and electronic interactions.

Introduction

Hydrogel, featuring a water-swollen three-dimensional polymer network, possesses a soft, elastic, and water-abundant nature that emulates the mechanical/chemical environment of biological tissue, making them one of the most ideal types of materials for interfacing with bio-tissues[1,6,7]. With their great chemical tunability and controllable porous framework, hydrogel functions as a versatile platform for supporting, treating, and communicating with bio-tissues, leading to a broad range of biointerfaced applications including cell culture medium, tissue engineering scaffolds[3,8,9], drug delivery[2,10], wound dressing[4,11], stimulation[12,13], and bio-monitoring[14,15].

An emerging biointerfaced technology is bioelectronics[16–22], which leverages the function sophistication and richness of electronics to probe and program biology with high accuracy and resolution. The development of bioelectronics centers around the realization of seamless, dynamic, and lasting interfaces between tissue and electronics, for which hydrogels stand as the unparalleled alternative to conventional electronic materials (i.e., conductors, semiconductors) for forming conformable tissue attachment[6], suppressing immune reactions[8], and efficient mass transport[23]. To fully exploit these capabilities of hydrogels, electronic and optoelectronic functions need to be embodied onto hydrogel designs. To this end, so far, only metallically conductive hydrogels have been reported, which are based on the design strategies of either swelled networks of conductive polymer PEDOT:PSS[24] or hydrogel composites with conductive fillers served by metallic nanofillers[25,26], 2D materials[27,28], or conjugated polymers[29]. However, the bioelectronic functions of such conductive hydrogels are only limited to electrode-based stimulation and passive sensing with moderate sensitivity. On the contrary, semiconductors, which feature electronic band structures with bandgaps, can enable much richer electronic and optoelectronic functions, including charge-transport modulation, amplification, photoexcitation, photo/electroluminescence, photocatalysis, etc (Fig. 1a). Therefore, imparting hydrogels with semiconducting properties is a

highly desirable but unmet need for enabling seamless biointerfaces to access a much broader range of advanced functions in sensing, stimulation, and imaging.

To realize semiconducting hydrogels with high electronic performance, polymer semiconductors[5,30] are arguably the most feasible choices for forming percolated 3D networks to achieve efficient charge transport. However, the main challenge comes from the incompatibility of the existing polymer semiconductors with the hydrogel preparation methods. Typically, hydrogels, including the reported conducting hydrogels, are formed through chemically or physically crosslinking the hydrogel precursors (i.e., either monomers or polymers) in water, which simultaneously retains a significantly water-swelled state. Such a process requires the aqueous processibility of hydrogel precursors. However, for polymer semiconductors, the vast majority of existing designs are only soluble in organic solvents. Although certain physical processing[31–33] and chemical modification[34] approaches have been used to enable aqueous processability, they typically either sacrifice the electrical performance or limit the accessibility of different electronic structures for diverse optoelectronic functions.

Here, we realized hydrogel semiconductors (hydro-SC) by devising a new processing method that decouples 3D network formation and water swelling into separate steps, which allowed the processing of common types of polymer semiconductors in organic solvents. This processing method produces a morphology with a polymer semiconductor forming a well-percolated network embedded in a porous hydrogel framework. Using an existing design of high-performance redox-active semiconducting polymer, the obtained hydrogel semiconductor gives not only high mobility (μ) (1.43 $cm^2 V^{-1} s^{-1}$) in organic electrochemical transistors (OECTs), but also tissue-level modulus (< 100 kPa). We show that such a significantly decreased modulus compared to all the existing polymer semiconductors indeed helps to achieve a suppressed foreign-body response (FBR) from chronic implantation. In addition, hydrogels' high porosity nature helps to enhance two biointerfaced functions of semiconductors. For optical stimulations, hydro-SC gives higher photoelectrochemical and photothermal effects compared to non-hydrogel films. For biosensing, hydrogels' diffusional permeability enables volumetric sensing of bulk-penetrated analytes, resulting in higher sensitivity compared to surface-based biosensing.

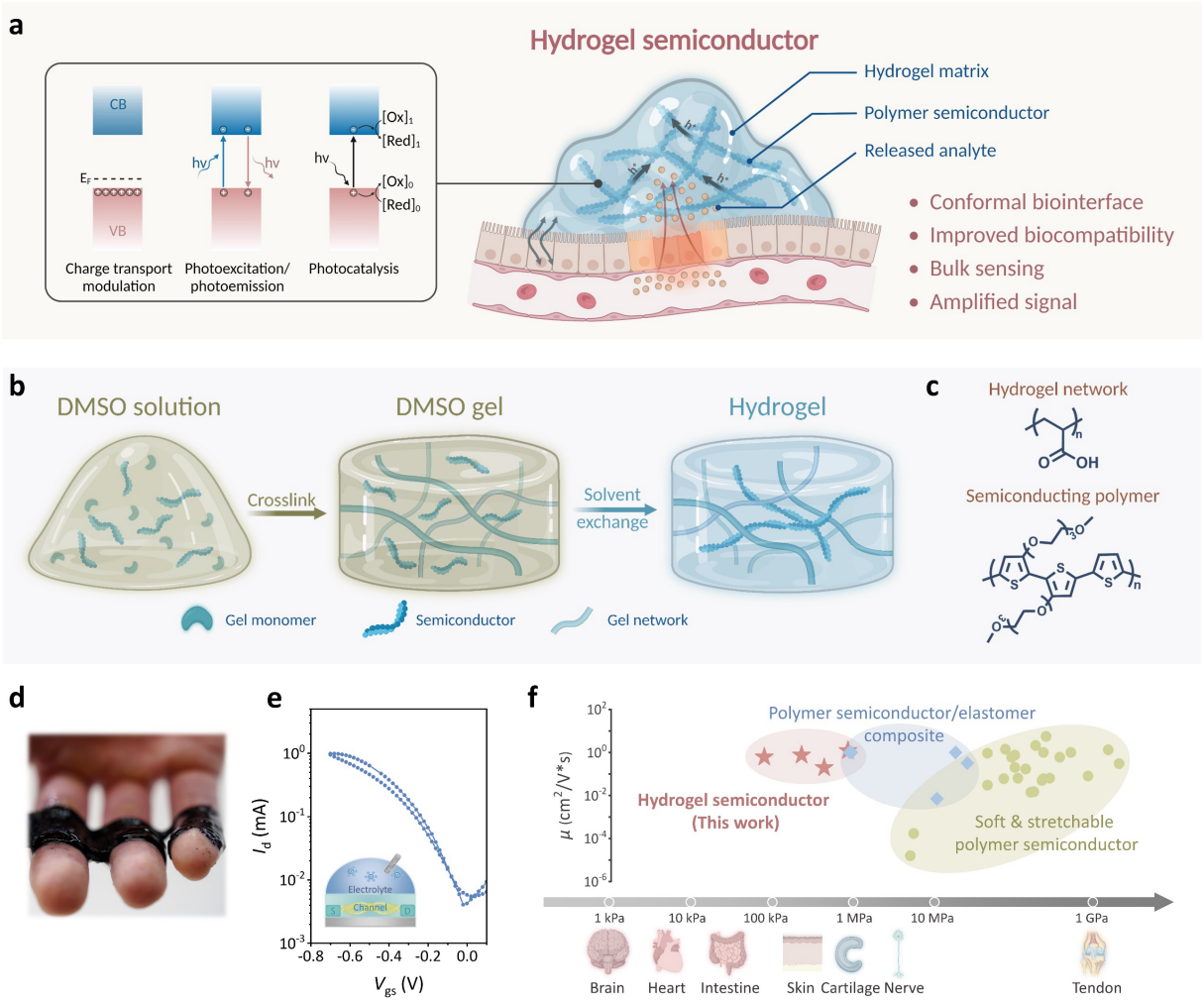

Fig. 1. Hydro-SC for bio-interfaced multi-modal applications. a, Design of hydro-SC based on interpenetrated double network of a semiconducting polymer and a hydrogel-forming polymers, which enables physically seamless, chemically boundaryless, and immune-compatible interfaces between bio-tissues and the advanced electronic and optoelectronic functions of semiconductors. **b,** Preparation method of the hydro-SC, which decouples the gelation step and water swelling step through solvent exchange. **c,** Chemical structures of the utilized hydrogel-forming polymer PAAc and semiconducting polymer p(g2T-T). **d,** Photograph showing a prepared hydro-SC conforms on the skin. **e,** Hydro-SC film serving as the channel layer in an OECT, giving normal transfer behavior (V_{ds} = -0.8 V). **f,** Comparisons of Young's moduli and charge-carrier mobility from the hydro-SCs (dark red) with other reported soft and stretchable semiconductors.

Design and processing method for hydro-SC

The design of the hydro-SC with an interpenetrated network (IPN) morphology comprises two main components: a polymer semiconductor with hydrophilic side chains, and a hydrogel-forming polymer (Fig. 1b). Our method to prepare hydro-SC (Fig. 1b) leverages the solubility of such a polymer semiconductor and the hydrogel-forming monomer in polar organic solvents such as DMSO. As such, the preparation of the hydro-SC starts from preparing a mixed solution of the polymer semiconductor and the hydrogel monomer in DMSO, together with the hydrogel crosslinker and photoinitiator. After spin-coating or casting the mixed solution into the desired form factor, UV-crosslinking is carried out to grow the 3D network of the hydrogel polymer (Supplementary Fig. 1), thereby inducing the gelation in DMSO. Finally, the gel is immersed in water to fully exchange DMSO with water (Supplementary Fig. 2), which turns the organogel into a hydrogel. During this process, since the polymer semiconductor is not soluble in water, we hypothesize that the semiconductor polymer will rapidly precipitate out and assemble into a percolated network inside the porous 3D hydrogel framework (Fig. 1b).

To implement this strategy, we chose poly (3,3'-bis(2-(2-(2-methoxyethoxy)ethoxy)ethoxy)2,2':5',2''-terthiophene) (p(g2T-T)) as the polymer semiconductor, and acrylic acid (AAc) as the hydrogel-forming monomer for its high reactivity in DMSO (Fig. 1c). With the initial concentrations of 20 mg/ml and 200 mg/ml in DMSO, we successfully prepared hydro-SCs that are ultrasoft with Young's modulus as low as 81.8 kPa, and can provide extraordinary conformability on the skin (Fig. 1d). When functioning as the channel layer in OECTs (Fig. 1e), the percolation of the semiconducting phase gives high μ of >1.2 $cm^2/V*s$. Compared to all the reported soft and stretchable polymer semiconductors, this hydro-SC realizes a decrease of the modulus over 2-3 orders of magnitude while keeping the μ at a similar level (Fig. 1f & Supplementary Table 1).

Characterization of the morphology evolvement during hydro-SC preparation

The key part of the design and preparation of the hydro-SC is the assembly process of the polymer semiconductor p(g2T-T) during the gelation and solvent exchange. To trace the morphological evolvement, we characterized three stages during the preparation process: the initial DMSO-based solution as stage 1, the UV-crosslinked gel in DMSO as stage 2, and the final hydro-SC after the

solvent exchange as stage 3 (Fig. 2a). For stage 1, cryogenic electron microscopy (cryo-EM) imaging of the rapidly frozen DMOS-based solution shows that the p(g2T-T) already formed high-density nano-aggregates (Fig. 2b, stage 1), likely attributed to the limited solvation of DMSO only on the polar side chains but not the hydrophobic backbones[35] (Supplementary Fig. 3). These pre-formed nano-aggregates could help to seed the further assembly of p(g2T-T) into larger networks. For stage 2, scanning electron microscopy (SEM) imaging on a frozen DMSO gel (Fig. 2b, stage 2) reveals that p(g2T-T) aggregates have merged into larger-size clusters (Fig. 2a, stage 2). Finally, water solvent exchange induces the assembly of p(g2T-T) into an interconnected network that is interpenetrated with the hydrogel polymer (i.e., poly(acrylic acid) (PAAc)) framework. Such a morphology is shown by SEM (Fig. 2b, stage 3 & Supplementary Fig. 4) in freeze-dried samples, and also conductive atomic force microscopy (c-AFM) on dried samples (Supplementary Fig. 5). This morphological evolvement process validated our hypothesis that the exchange to a non-solvent (i.e., water) drives the assembly of polymer semiconductor chains into a percolated network for enabling long-range charge transport.

To probe deeper into the molecular level percolation of the polymer semiconductors during the process, we further measured the charge-transport performance by utilizing each stage of the solution/gel to make OECT devices. By performing our hydrogel preparation process on substrates with pre-deposited gold electrodes, the semiconductor solution/gel at each stage can serve as the OECT channel (Fig. 2c). For stages 1 and 2, we utilize the electrolyte with DMSO solvent and organic choline chloride (Ch^+Cl^-) salt, which is added on top of the DMSO solution/gel in these two stages to enable sufficient penetration of the ions into the semiconducting channel layers (Supplementary Note 1). Surprisingly, stage 1 already gave high electrical performance with the G_m of 8.54 mS (Fig. 2d & Supplementary Fig. 6a), indicating that molecular-level percolation of p(g2T-T) already exists in the solution state in DMSO. Then, after the UV cross-linking of the hydrogel polymer in DMSO (i.e., stage 2), the electrical performance decreased by about two orders of magnitude (Fig. 2d & Supplementary Fig. 6b), suggesting that the crosslinking of the AAc monomer breaks the molecular-level percolation of p(g2T-T). After the solvent exchange, the formation of the microscopic p(g2T-T) fiber network in the final hydro-SC reverted the electrical performance to a similar level with stage 1, as shown by the OECT measurement (Fig. 2d & Supplementary Fig. 6c) using aqueous choline chloride electrolyte.

For the hydro-SC thin film, we further studied the polymer packing of p(g2T-T). Grazing-incidence X-ray diffraction (GIXD) (Fig. 2e) shows that, in contrast to a neat p(g2T-T) film deposited from chloroform solution, the hydro-SC film does not have observable crystalline features (Fig. 2e & f). This suggests that the formation of long-range ordering is suppressed during the rapid polymer chain precipitation from the solvent exchange process, together with the inhibition effect of the PAAc network. On the other hand, UV-vis spectroscopy reveals enhanced short-range aggregation in hydro-SC films (Fig. 2g), as evidenced by the higher (0-1)/(0-0) ratio than that from p(g2T-T) films. We reason that the higher aggregation level comes from the stronger aggregation of p(g2T-T) in DMSO solvent, compared to the dissolution in chloroform. Overall, such a packing morphology could be an optimal balance for the hydro-SC with duality design goals: on one hand, the enhanced local aggregation and the microstructure-level percolation can ensure efficient interchain charge transport, and on the other hand, the lack of crystallization can help to achieve softer mechanical properties. For the electronic structures, we also utilized cyclic voltammetry (Supplementary Fig. 7) and UV-vis to confirm that the HOMO and LUMO levels of hydro-SC are almost identical to those of p(g2T-T), which give similar redox activities under electrochemical biasing (Supplementary Fig. 8).

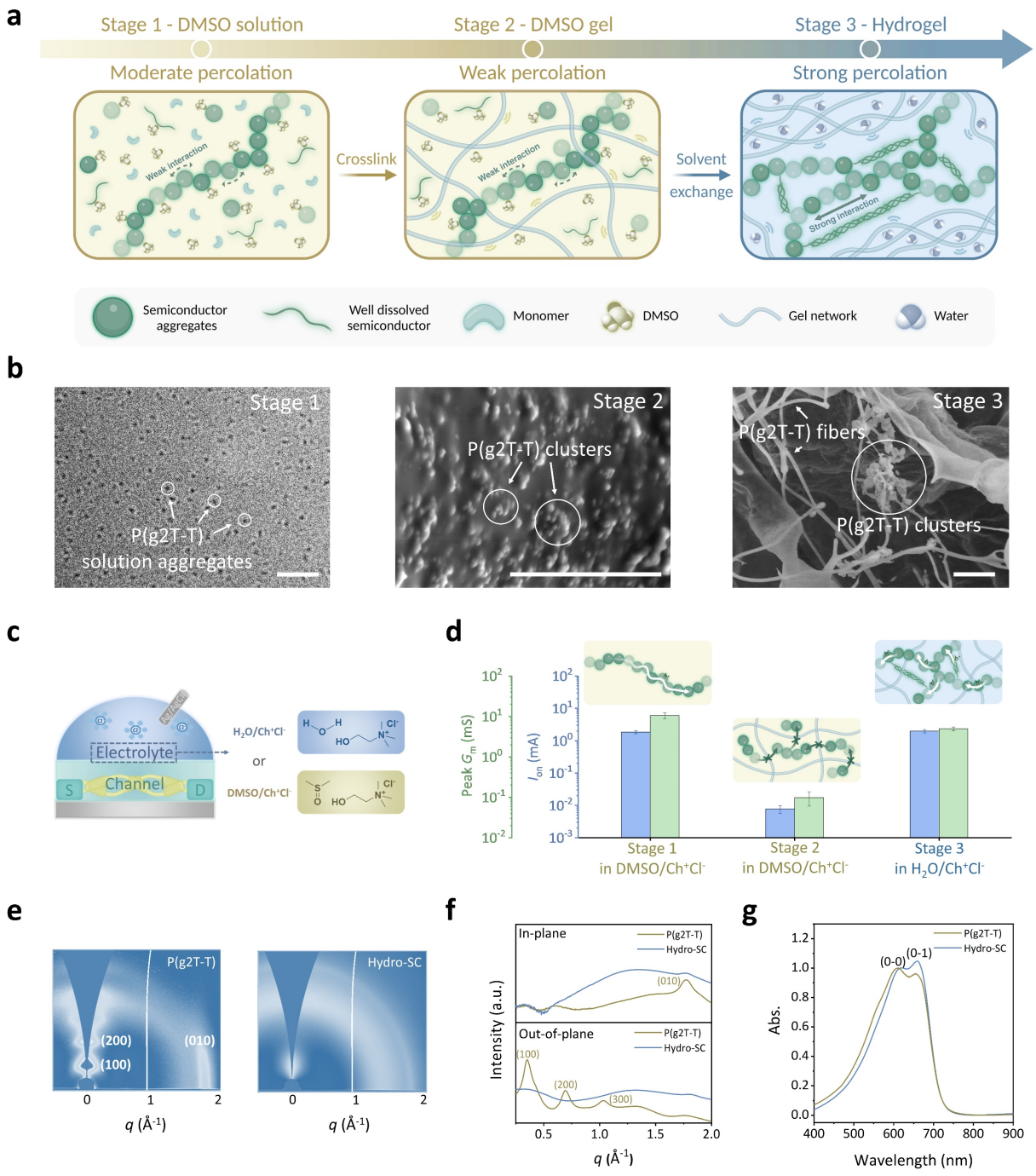

Fig. 2 Morphology evolvement during the formation of hydro-SC. a, Schematics showing the morphology evolvement during the three stages of the hydro-SC preparation, highlighting the aggregation and network-formation process of p(g2T-T). **b,** Cryo-EM (stage 1) and SEM images (stage 2 & 3) of hydro-SC at different stages (scale bars, 2 μm), showing the existence of p(g2T-T) aggregates in the initial DMSO solution, the growth of the aggregates into clusters after UV

crosslinking, and the formation of the interconnected network after solvent exchange in water. **c, d**, OECT tests in two types of electrolytes (i.e., Ch^+Cl^- in DMSO, and Ch^+Cl^- in water) (**c**), and electrical performance of hydro-SC at each of the preparation stages (**d**), revealing the molecular level percolation of p(g2T-T) (n = 3 independent measurements). **e,** 2D GIXD images of a neat p(g2T-T) film and a hydro-SC film. **f,** 1D-linecuts in the in-plane and out-of-plane directions of the neat p(g2T-T) and hydro-SC film. **g,** Normalized UV-vis spectrums of a neat p(g2T-T) film and a hydro-SC film. Both films were electrochemically de-doped to -0.2 V vs. Ag/AgCl during the measurement.

Electrical and mechanical properties of hydro-SC

For the hydro-SC design, there are mainly two compositional factors that can influence both the electrical and mechanical properties: the crosslinking level of the PAAc network, and the weight ratio between PAAc and p(g2T-T). We first compare the electrical performance in OECT devices (Fig. 3a). The influence of crosslinking density was tested by varying the crosslinker weight percentage among 0.2%, 0.5%, and 2% of the AAc monomer, with the p(g2T-T)-to-AAc weight ratio kept at 10/100. With all three compositions showing ideal OECT transfer and output behaviors (Fig. 3b & Supplementary Fig. 9), the lowest crosslinking ratio gives the highest μ of 1.22 $cm^2/V*s$ (Fig. 3c & Supplementary Fig. 10). This is possibly due to the elevated suppression of the ordered assembling of p(g2T-T) by a denser PAAc network. The slightly higher μ from 2% crosslinker than 0.5% could come from the lower swellability of the hydrogel with a higher crosslinking ratio (Supplementary Note 2 & Supplementary Fig. 11). This is evidenced by the comparison of the OECT performance from the hydro-SC in the dry state, by utilizing ion-exchange gel as the electrolyte[36] (Supplementary Fig. 12). On the other hand, when we increase the p(g2T-T)-to-PAAc weight ratio from 5/100 to 13.3/100 while the crosslinker concentration is kept at 0.2% (Supplementary Table 2 & Supplementary Fig. 13), we see a substantial increase of the μ from a non-measurable level to 1.43 $cm^2\ V^{-1}\ s^{-1}$ (Fig. 3d & Supplementary Fig. 14), which should come from a better percolation of the p(g2T-T) network.

We next study the mechanical properties of the hydro-SC thin film through floating-on-water (FoW) tensile test[37] (Fig. 3e). The films are in the swelled state on the supporting liquid, for which

we utilized an aqueous electrolyte of 0.1 M NaCl to emulate the physiological environment. compared to water, such an electrolyte environment will lead to less swelling and slightly higher modulus. As shown in Fig. 3f and Supplementary Fig. 15, the gradual increase of the crosslinking density first leads to a decrease and then an increase of the modulus, which should come from the combined effect of the increase in both network density and swellability. The increased weight ratio of p(g2T-T) consistently gives a high modulus, simply due to the increased percentage of the more rigid component (Fig. 3g & Supplementary Fig. 16). For the lowest modulus of 81 kPa achieved from hydro-SCs, it is a decrease by more than 3 orders of magnitude than the pristine p(g2T-T) (Fig. 3g). Besides, the hydro-SC also exhibit much higher stretchability than p(g2T-T) (Supplementary Fig. 17). Supported on polystyrene-block-poly (ethylene-ran-butylene)-block-polystyrene (SEBS) substrates, hydro-SC (0.5% crosslinking, 10/100 ratio) films can be stretched up to 150% strain without crack formation or OECT performance degradation (Fig. 3h & Supplementary Fig. 18).

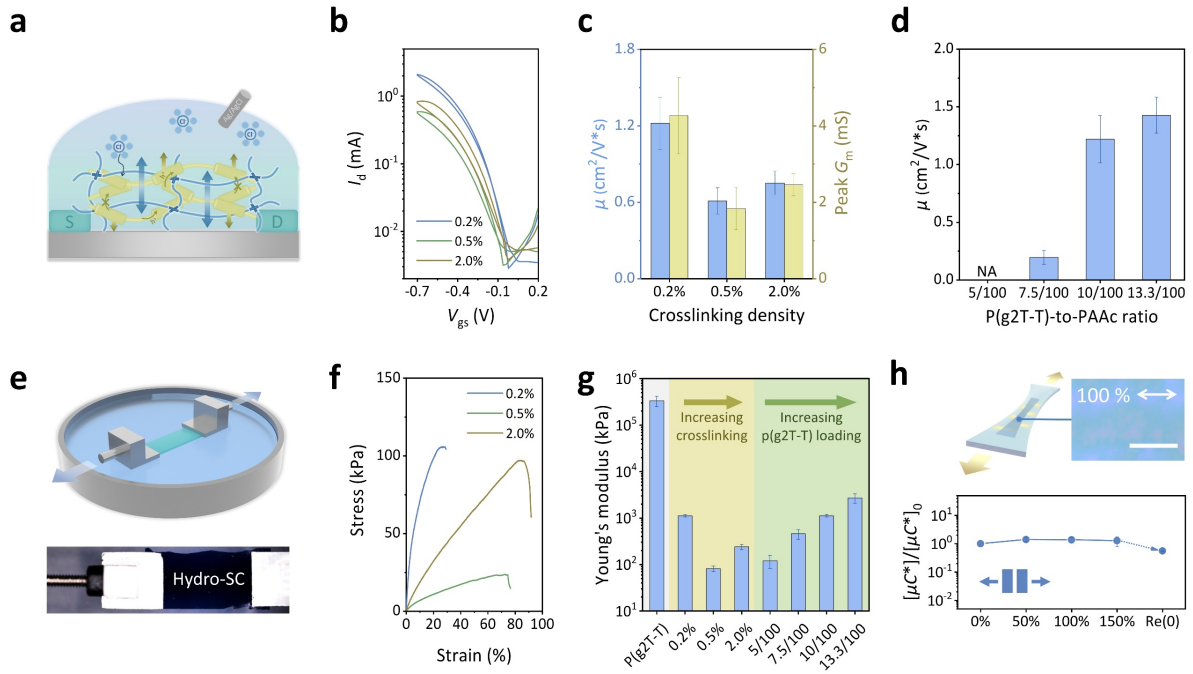

Fig. 3 Electrical and mechanical properties of hydro-SC films. a, OECT tests using swelled hydro-SC films. **b, c,** OECT transfer curves (**b**), extracted charge-carrier mobility (μ), and peak transconductance (G_m) (**c**) from hydro-SCs with three different crosslinking ratios (V_{ds} = -0.8 V). (n = 9 independent measurements). **d,** Extracted μ's from hydro-SCs with different p(g2T-T)-to-

AAc weight ratios (n = 9 independent measurements). **e,** Schematic (top) and picture (bottom) showing the FOW test for the tensile properties of hydro-SC films. **f,** Stress-strain curves of hydro-SC films with different crosslinking ratios. **g,** Young's moduli of p(g2T-T) and hydro-SC films with different p(g2T-T)-to-AAc weight ratios (n = 4 independent measurements). **h,** Stretchability test of hydro-SC films on a SEBS substrate with D/S electrodes (top), with the optical microscopy image showing the morphology under 100% strain (scale bar, 20 μm), and normalized μC^* from OECT measurements during the stretching to 150% strain (in parallel to the charge transport direction) and release (n = 9 independent measurements).

Hydro-SC for bio-interfacing: higher conformability and lower immune responses

For the use of hydro-SC to interface with bio-tissues or skins, the first advantage is the higher conformability from the ultralow modulus[38]. As demonstrated by adhering a hydro-SC film (10 μm thick) on a tendon replica with a rough and irregular surface (Fig. 4a), the film very well adapted to the original surface morphology (Fig. 4b & Supplementary Fig. 19a). In contrast, for neat p(g2T-T) film, though much thinner (~100 nm), the lamination failed to conform to most of the surface features and left significant gaps in between (Fig. 4c & Supplementary Fig. 19b).

The second advantage of the tissue-level modulus of hydro-SC thin films is the suppressed FBR[39]. This was tested by coating different films on both sides of SEBS substrates and implanting subcutaneously in mice for 4 weeks. On the explanted tissues around the implants (Supplementary Fig. 20 & 21), Masson's trichrome staining (Fig. 4d) shows that the hydro-SC films with 2.0% crosslinker and a modulus of 239 kPa had clearly reduced collagen densities compared to both the bare SEBS implants and the p(g2T-T) films. The level of the collagen density is already comparable to that of PAAc hydrogel, which has a modulus of 12.8 kPa (Supplementary Fig. 22a). Such an effect of Young's modulus on the FBR was further validated by hydro-SC films with much higher crosslinking ratios (10%), and thereby higher modulus of 4.76 MPa (Supplementary Fig. 22b). The collagen density level is clearly higher than the softer hydro-SC, and actually stays on the similar level with the neat p(g2T-T) films (Fig. 4e). Such an influencing behavior of surface modulus on the FBR level is consistent with previous studies on hydrogels and elastomers[40,41].

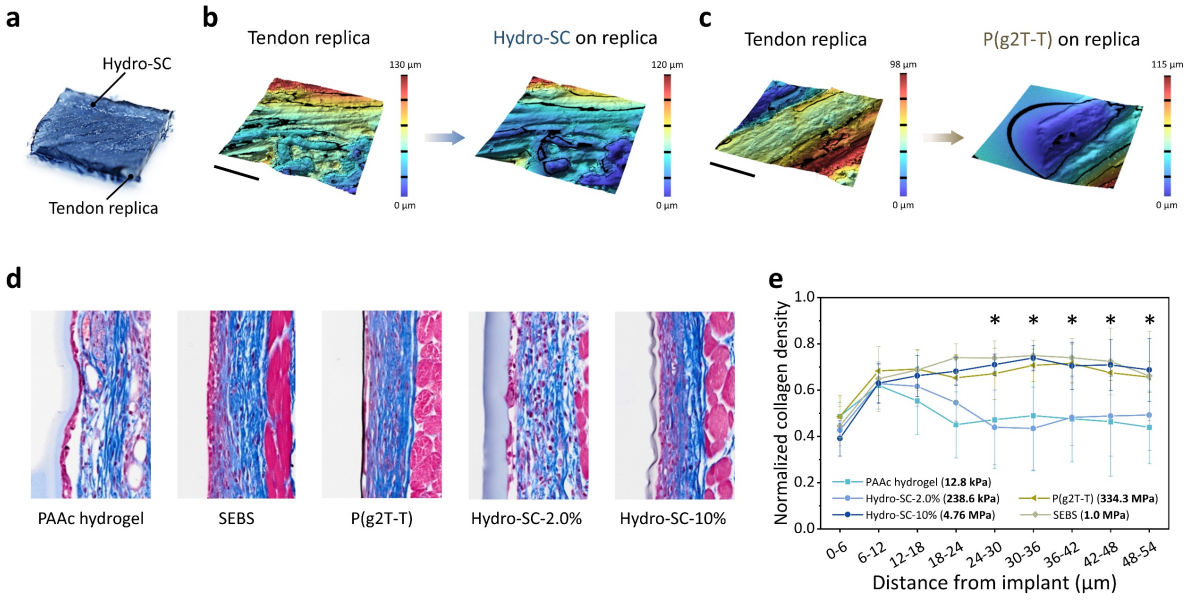

Fig. 4 Hydro-SC interfacing with bio-tissues with increased conformability and suppressed FBR. a, Picture showing a hydro-SC film laminated on a piece of tendon replica. **b,** 3D height profile images of tendon replica before and after the lamination of the hydro-SC film. **c,** 3D height profile images of tendon replica before and after the lamination of a neat p(g2T-T) film, as a comparison. Scale bars, 200 μm. **d,** Masson's trichrome staining results of tissues around five types of implants after 4 weeks of subcutaneous implantation in mice. **e,** Normalized collagen density of different implants as the function of distance (n = 6 independent measurements). Statistical significance and P values are determined by two-sided Student's t-test: * $P < 0.05$.

Hydro-SC giving enhanced photo-modulation effects

Semiconductors have been demonstrated with photo-modulation functions for biointerfaces applications, through photoelectrochemical, photothermal, and photocapacitive effects. We first studied the photoelectrochemical behavior (Fig. 5a) of hydro-SC using a patch-clamp setup under physiological conditions[17] (Fig. 5b). When irradiated by a 625 nm laser, the hydro-SC film showed a clear faradic current, which indicates the charge transfer happening between semiconductor and electrolyte (Fig. 5c & Supplementary Fig. 23). The stabilized current level is substantially higher than a neat p(g2T-T) film (of the same weight with the p(g2T-T) component in the hydro-SC film) tested under the same condition (Fig. 5c). Further calculation reveals that the hydro-SC design

improved the charge injection by nearly 20-folds (Fig. 5d). We reason that this is mostly attributed to the porous nature of the hydrogel design that largely increases the semiconductor-electrolyte interfaces for more efficient use of electrons/holes by redox reactions[42].

We next studied the photo-thermal properties that come from the non-radiative decay following photoexcitation (Fig. 5e). Under a radiation power of 205 mW/cm^2, a hydro-SC film (in the dry state for more accurate temperature measurement) reached to 90°C within 15 seconds (Fig. 5f & Supplementary Fig. 24). The temperature level has a positive relationship with the radiation power. Under the same radiation condition, the hydro-SC film achieved a higher temperature than a neat p(g2T-T) film (Fig. 5g & Supplementary Fig. 25). Hypothetically, such stronger photothermal effect from hydro-SC might come from the stronger aggregation level as shown earlier (Fig. 2g), which increases the non-radiative decay coming from π-π stacking[43]. When used applied on bio-tissue (e.g., pig skin) surfaces covered with biofluids, the hydro-SC in the fully swelled state can also generate rapid heating with the temperature reaching 90°C in 30 s, under a low radiation power of 318 mW/cm^2 (Fig. 5h). As such, for therapeutic applications, our hydro-SC could be an ideal type of dressing layer for wound healing processes, which combines efficient photothermal treatment, and hydrogels' benefits of ultrasoft modulus, oxygen permeability, moisturization on wound surfaces (Fig. 5i).

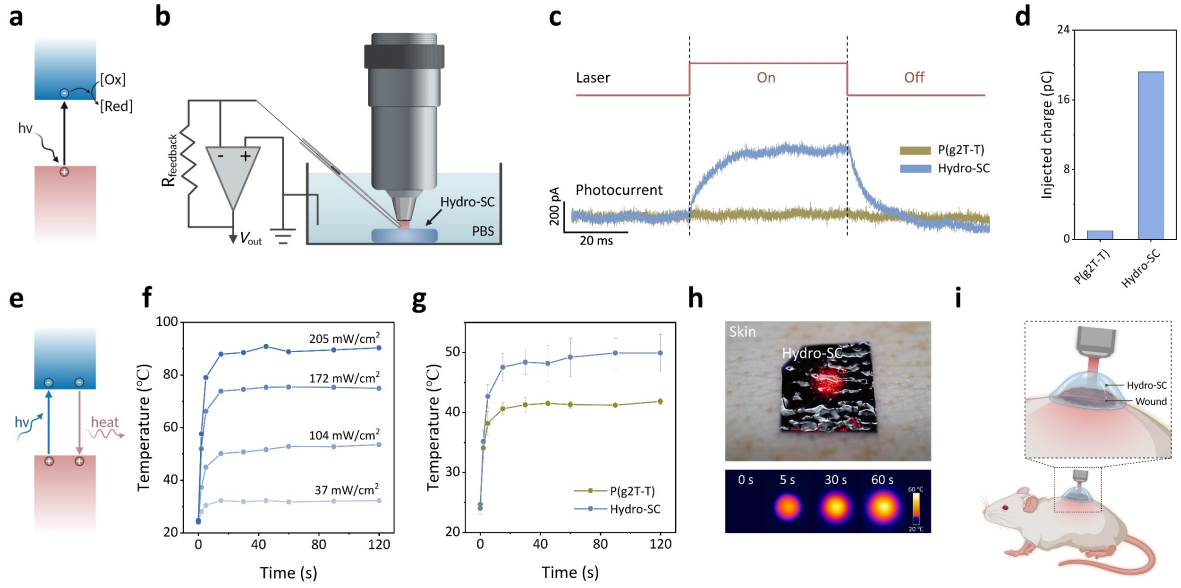

Fig. 5. Enhanced photo-modulation effects from hydro-SC. a, Mechanism of the photoelectrochemical effect from semiconductors. **b,** Test setup for photoelectrochemical measurement. **c,** Photoelectrochemical response of hydro-SC and p(g2T-T) films, under the radiation power of 4.5 W/cm^2. The amount of p(g2T-T) was kept same in both films. **d,** Calculated amounts of charges injected into both films during radiation. **e,** Mechanism of the photothermal effect from semiconductors. **f,** Photothermal response of a hydro-SC film (in the dry state) under different radiation powers. **g,** Comparison of photothermal response of a hydro-SC film and a neat p(g2T-T) film. The amount of p(g2T-T) was kept same in both films. Radiation power, 104 mW/cm^2. **h,** Photothermal heating from a hydro-SC film applied on a piece of wet pig skin. Radiation power, 318 mW/cm^2. **i,** Application of hydro-SC as wound dressing for providing thermotherapy.

Bulk-diffusion-enabled volumetric biosensing

Another key biointerfaced applications for the hydro-SC is biochemical sensing, e.g., through OECT devices. Biochemical sensing can particularly benefit from the bulk mass transport properties of hydrogels. For existing polymer semiconductors, the dense nature and limited hydrophilicity can hardly allow the transport of biomolecules into the bulk volume. As a result, both the functionalization of bioreceptors and the sensing of bioanalytes can only happen at the surface (Fig. 6a). This has been the sensing mode for all the transistor-type biosensors[44–47]. For our hydro-SC, the mass transport properties for biomolecules now could open up the possibility for volumetric sensing (Fig. 6a) throughout the entire thickness of the semiconducting layer. We reason that such volumetric sensing can enable many more interaction sites between bioreceptors and analyte molecules, and thereby higher sensitivity. To test this possibility, we first utilized fluorescent imaging to directly visualize the diffusion capability of large-sized molecules through a hydro-SC film-based membrane (Fig. 6b). This experiment was carried out using a macromolecular fluorescent probe PEG-FITC (M_n = 20 kDa, Supplementary Fig. 26), which emulates the molecular sizes of proteins and nucleic acids. As shown in Fig. 5c, the fluorescence probes, initially on one side of the hydro-SC membrane, diffused to the other side after 24 hours. In comparison, for a membrane made from a neat p(g2T-T) film, such diffusion cannot be observed (Fig. 6c and Supplementary Fig. 27).

To further realize volumetric biosensing, a key requirement is to have a method to functionalize bioreceptors throughout the bulk of hydro-SC. We designed an approach that utilizes crosslinking to immobilize the penetrated bioreceptor molecules in the hydro-SC layer (Supplementary Fig. 28). Specifically, one possible chemistry to realize such crosslinking is by utilizing glutaraldehyde as the crosslinker to react with amine groups that universally exist in proteins[48]. To demonstrate this approach, we employed glucose oxidase (GOx) as an enzymatic bioreceptor. The hydro-SC utilized in this experiment was prepared with poly(acrylamide) (PAAm) as the hydrogel forming polymer because of its electrical neutrality. After 24 hours of incubation in GOx solution with the crosslinker, the successful immobilization of GOx throughout the thickness of the hydro-SC film can be confirmed through X-ray photoelectron spectroscopy (XPS) depth profiling (Fig. 6d & e) on wash-dried samples. In this analysis, the C1s peak from GOx was used due to the overlap of the stronger N1s peak with PAAm (Fig. 6d & Supplementary Fig. 29). In contrast, the same functionalization process performed on a neat p(g2T-T) only leads to the immobilization of GOx on the surface (Fig. 6f & g), which is due to the limited infiltration of GOx into the p(g2T-T) film.

We further tested the volumetric sensing performance of the bulk-functionalized hydro-SC in an OECT device, which was compared with surface-functionalized p(g2T-T) film. For glucose analyte, the sensing can happen through glucose oxidation at the active site of GOx, which leads to the reduction of oxygen to hydrogen peroxide that further oxidizes the p(g2T-T) (Fig. 6h). For hydro-SC, the gradual increase of the drain current (I_d) can be observed during the increase of the glucose concentration from 100 nM to 2 mM (Fig. 6i). By analyzing the relationship between the shift of threshold voltage (V_{th}) with the glucose concentration (Fig. 6j), the detection limit can be determined as 500 nM. In comparison, the surface functionalized p(g2T-T) only shows current decrease when the glucose concentration is higher than 100 μM (Fig. 6k), which could come from the electrooxidation of glucose[49](Supplementary Fig. 30), indicating the surface-immobilized GOx is insufficient to achieve considerable enzymatic reactions (Supplementary Fig. 31). Overall, this comparison validated that the volumetric biosensing achieved through the hydro-SC can be a highly effective strategy for increasing the sensitivity.

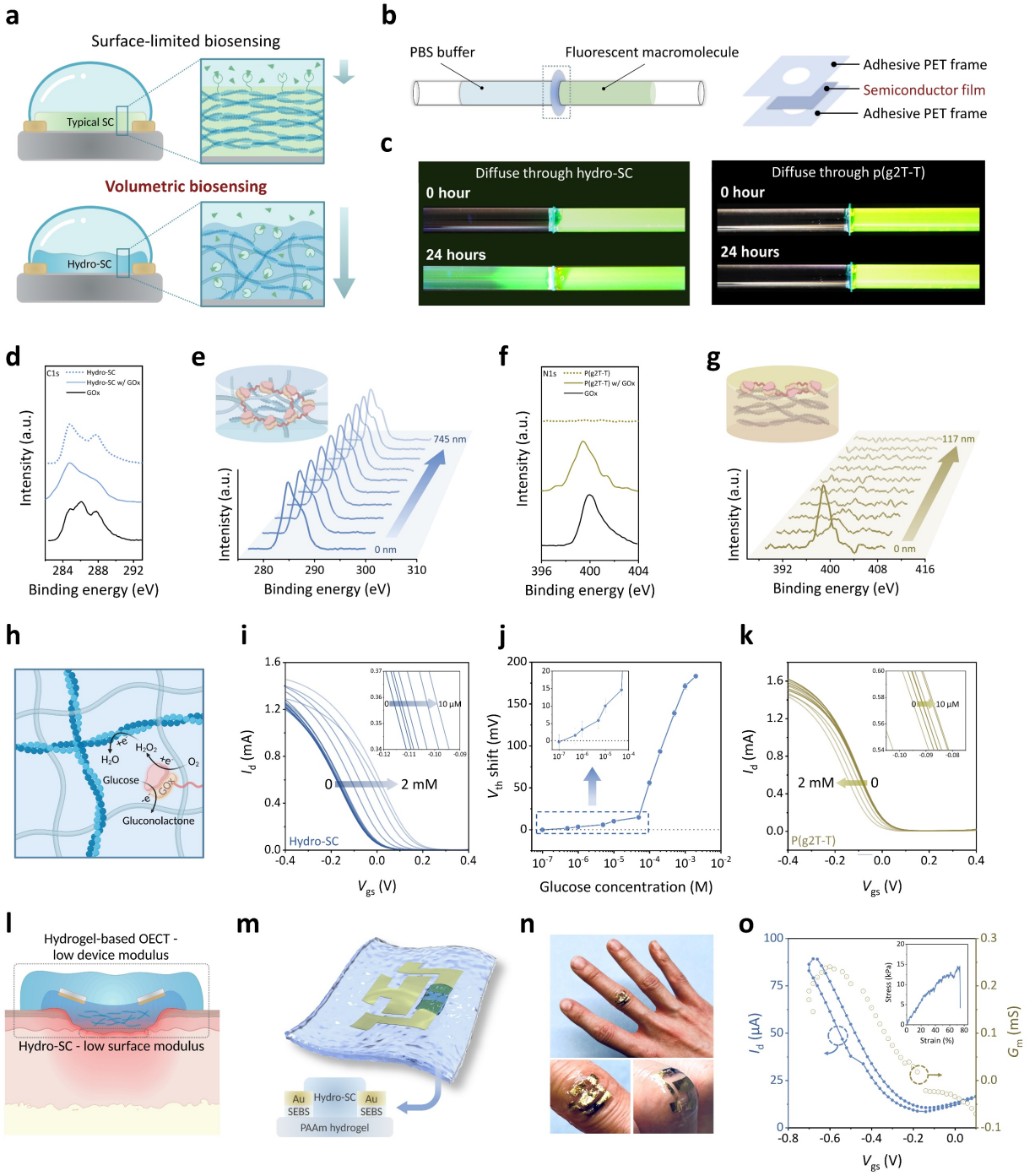

Fig. 6. Biosensing using hydro-SC: volumetric sensing with higher sensitivity and hydrogel-based OECT devices with tissue-like modulus. a, Schematics comparing the mechanism of conventional surface-limited biosensing (bottom) and volumetric biosensing (top), showing that volumetric biosensing provides more interaction sites with analytes. **b,** Setup for qualitatively testing the diffusion ability of semiconductor films by large molecules, in which a semiconducting

film serves as the membrane with fluorescent probe molecules initially only on one side of the membrane. **c,** Diffusion of fluorescent probes through hydro-SC (left) and neat p(g2T-T) (right) films in 24 hours. **d,** C1s spectra of XPS characterizations on GOx alone, a hydro-SC film without GOx immobilization, and a hydro-SC film with GOx immobilization. **e,** C1s spectra of XPS depth profiling through the thickness of a hydro-SC film after GOx immobilization. **f,** N1s spectra of XPS characterizations on GOx alone, a neat p(g2T-T) film without GOx immobilization, and a neat p(g2T-T) film with GOx immobilization. **h,** Sensing response mechanism in hydro-SC during volumetric sensing of glucose. **i,** Volumetric sensing performance for glucose from a hydro-SC as the channel layer in an OECT device. **j,** Correlation between the threshold voltage (V_{th}) shifts and glucose concentrations (n = 3 independent measurements). **k,** Surface sensing performance for glucose from a neat p(g2T-T) film as the channel layer in an OECT device. **l,** Schematic showing a hydrogel-based OECT (hydro-OECT) for interfacing with bio-tissues with tissue-like moduli both on the device surface and from the whole device. **m,** Device structure of a hydro-OECT. **n,** Photographs of a hydro-OECT device on a bending finger joint, showing highly conformable contact. **o,** Modulus measurement (inset) and electrical performance of a hydro-OECT.

Hydrogel-based OECTs

For the application of such OECT-based biosensing with direct interfacing with bio-tissues, the requirement on tissue-level softness is mainly composed of two aspects: the surface modulus that is in direct contact with the tissue, and the effective modulus of the full device (Fig. 6l). The use of our hydro-SC as the sensing surface can satisfy the former part. To further fulfill the latter part, we utilized the hydro-SC to create stretchable OECT devices on an ultrasoft hydrogel substrate (Fig. 6m and Supplementary Fig. 32). In our design, the stretchable electrodes were served by microcracked gold films[50], which were on a thin layer of SEBS sitting on top of the hydrogel substrate. The SEBS layer not only forms interpenetrated interface with the gold films to enable the microcrack morphology, but also prevents shorting of the electrodes by water in the hydrogel. The obtained hydrogel-based OECT gives very high conformability even on a highly wrinkled part of the skin (Fig. 6n), which is benefited from the ultralow modulus of ~30.9 kPa (the inset of Fig. 6o). Together with the ideal transistor performance (Fig. 6o), this device provides the most ideal mechanical and electrical properties for interfacing with bio-tissues.

Conclusions

Our interpenetrated-double-network design for hydrogel semiconductors have successfully united high-performance semiconducting properties with hydrogels' unique features, including tissue-like softness, high porosity, and efficient transport of biomolecules. We showed that these hydrogel properties greatly improved the conformability and immune compatibility for the use of semiconductors on tissue surfaces. In addition, the highly porous morphology with high surface aspect ratio of the hydrogel design also enhanced some of the bioelectronic functions of semiconductors, such as biosensing with higher sensitivity through unprecedented volumetric sensing, and stronger photoelectrochemical and photothermal effects for optical stimulation. All these are enabled by a new solvent-exchange processing method for hydrogels, which circumvents the need of water processibility for semiconducting polymers. Moving forward, this method offers broad applicability to different designs of redox-active semiconducting polymers, so that hydrogel designs can be achieved on different semiconductor-based functions that need different band structures. We envision that hydrogel semiconductors that blur the mechanical and chemical interfaces between semiconductors and bio-tissues can play a central role in bridging electronics technologies with hydrogel-based biomedical technologies.

References

1. Yuk, H., Lu, B. & Zhao, X. Hydrogel bioelectronics. *Chemical Society Reviews* (2018) doi:10.1039/c8cs00595h.

2. Li, J. & Mooney, D. J. Designing hydrogels for controlled drug delivery. *Nat. Rev. Mater.* **1**, 16071 (2016).

3. Lee, K. & Mooney, D. J. Hydrogels for Tissue Engineering. *Chemical Reviews* **101**, 1869–1880 (2001).

4. Liang, Y., He, J. & Guo, B. Functional Hydrogels as Wound Dressing to Enhance Wound Healing. *ACS Nano* **15**, 12687–12722 (2021).

5. Ding, L. *et al.* Polymer Semiconductors: Synthesis, Processing, and Applications. *Chem. Rev.* (2023) doi:10.1021/acs.chemrev.2c00696.

6. Yuk, H., Wu, J. & Zhao, X. Hydrogel interfaces for merging humans and machines. *Nat. Rev. Mater.* **7**, 935–952 (2022).

7. Daly, A. C., Riley, L., Segura, T. & Burdick, J. A. Hydrogel microparticles for biomedical applications. *Nat Rev Mater* 1–24 (2019) doi:10.1038/s41578-019-0148-6.

8. Naahidi, S. *et al.* Biocompatibility of hydrogel-based scaffolds for tissue engineering applications. *Biotechnol. Adv.* **35**, 530–544 (2017).

9. Lou, J. & Mooney, D. J. Chemical strategies to engineer hydrogels for cell culture. *Nat. Rev. Chem.* **6**, 726–744 (2022).

10. Shi, J. *et al.* Monolithic-to-focal evolving biointerfaces in tissue regeneration and bioelectronics. *Nat. Chem. Eng.* **1**, 73–86 (2024).

11. Zhang, L., Liu, M., Zhang, Y. & Pei, R. Recent Progress of Highly Adhesive Hydrogels as Wound Dressings. *Biomacromolecules* **21**, 3966–3983 (2020).

12. Deng, J. *et al.* Electrical bioadhesive interface for bioelectronics. *Nat Mater* 1–8 (2020) doi:10.1038/s41563-020-00814-2.

13. Guimarães, C. F., Ahmed, R., Marques, A. P., Reis, R. L. & Demirci, U. Engineering Hydrogel-Based Biomedical Photonics: Design, Fabrication, and Applications. *Adv. Mater.* **33**, e2006582 (2021).

14. Zhu, T. *et al.* Recent advances in conductive hydrogels: classifications, properties, and applications. *Chem. Soc. Rev.* **52**, 473–509 (2022).

15. Ma, J. *et al.* Hydrogel sensors for biomedical electronics. *Chem. Eng. J.* **481**, 148317 (2024).

16. Dai, Y., Hu, H., Wang, M., Xu, J. & Wang, S. Stretchable transistors and functional circuits for human-integrated electronics. *Nat Electron* **4**, 17–29 (2021).

17. Li, P. *et al.* Monolithic silicon for high spatiotemporal translational photostimulation. *Nature* **626**, 990–998 (2024).

18. Jiang, Y. *et al.* Topological supramolecular network enabled high-conductivity, stretchable organic bioelectronics. *Science* **375**, 1411–1417 (2022).

19. Wang, C. *et al.* Bioadhesive ultrasound for long-term continuous imaging of diverse organs. *Science* **377**, 517–523 (2022).

20. Liu, J. *et al.* Bioresorbable shape-adaptive structures for ultrasonic monitoring of deep-tissue homeostasis. *Science* **383**, 1096–1103 (2024).

21. Hu, H. *et al.* A wearable cardiac ultrasound imager. *Nature* **613**, 667–675 (2023).

22. Strakosas, X. *et al.* Metabolite-induced in vivo fabrication of substrate-free organic bioelectronics. *Science* **379**, 795–802 (2023).

23. Axpe, E. *et al.* A Multiscale Model for Solute Diffusion in Hydrogels. *Macromolecules* (2019) doi:10.1021/acs.macromol.9b00753.

24. Lu, B. *et al.* Pure PEDOT:PSS hydrogels. *Nature Communications* **10**, 1043 (2019).

25. Ohm, Y. *et al.* An electrically conductive silver–polyacrylamide–alginate hydrogel composite for soft electronics. *Nat Electron* **4**, 185–192 (2021).

26. Dvir, T. *et al.* Nanowired three-dimensional cardiac patches. *Nature Nanotechnology* **6**, 720 (2011).

27. Lu, Y. *et al.* Stretchable graphene–hydrogel interfaces for wearable and implantable bioelectronics. *Nat. Electron.* **7**, 51–65 (2024).

28. Song, H. S., Kwon, O. S., Kim, J.-H., Conde, J. & Artzi, N. 3D hydrogel scaffold doped with 2D graphene materials for biosensors and bioelectronics. *Biosens. Bioelectron.* **89**, 187–200 (2017).

29. Liu, D. *et al.* Conductive polymer based hydrogels and their application in wearable sensors: a review. *Mater. Horiz.* **10**, 2800–2823 (2023).

30. Zheng, Y., Zhang, S., Tok, J. B.-H. & Bao, Z. Molecular Design of Stretchable Polymer Semiconductors: Current Progress and Future Directions. *J. Am. Chem. Soc.* **144**, 4699–4715 (2022).

31. Wu, J. *et al.* Semiconducting Polymer Nanoparticles for Centimeters-Deep Photoacoustic Imaging in the Second Near-Infrared Window. *Advanced Materials* **29**, 1703403 (2017).

32. Sim, K. M. *et al.* Surfactant-Induced Solubility Control To Realize Water-Processed High-Precision Patterning of Polymeric Semiconductors for Full Color Organic Image Sensor. *ACS Nano* **14**, 415–421 (2020).

33. Cho, J. *et al.* Universal selection rule for surfactants used in miniemulsion processes for eco-friendly and high performance polymer semiconductors. *Energy Environ. Sci.* **10**, 2324–2333 (2017).

34. Marcial-Hernandez, R. *et al.* Aqueous processing of organic semiconductors enabled by stable nanoparticles with built-in surfactants. *Nanoscale* **15**, 6793–6801 (2023).

35. Xu, Z. *et al.* Not All Aggregates are Made the Same: Distinct Structures of Solution Aggregates Drastically Modulate Assembly Pathways, Morphology and Electronic Properties of Conjugated Polymers. *Adv Mater* 2203055 (2022) doi:10.1002/adma.202203055.

36. Bischak, C. G., Flagg, L. Q. & Ginger, D. S. Ion Exchange Gels Allow Organic Electrochemical Transistor Operation with Hydrophobic Polymers in Aqueous Solution. *Adv Mater* **32**, 2002610 (2020).

37. Galuska, L. A. *et al.* SMART transfer method to directly compare the mechanical response of water-supported and free-standing ultrathin polymeric films. *Nat Commun* **12**, 2347 (2021).

38. Yan, Z. *et al.* Highly stretchable van der Waals thin films for adaptable and breathable electronic membranes. *Science* **375**, 852–859 (2022).

39. Capuani, S., Malgir, G., Chua, C. Y. X. & Grattoni, A. Advanced strategies to thwart foreign body response to implantable devices. *Bioeng. Transl. Med.* **7**, e10300 (2022).

40. Li, N. *et al.* Bioadhesive polymer semiconductors and transistors for intimate biointerfaces. *Science* **381**, 686–693 (2023).

41. Ni, Y. *et al.* Macrophages modulate stiffness-related foreign body responses through plasma membrane deformation. *Proc. Natl. Acad. Sci.* **120**, e2213837120 (2023).

42. Chang, C.-L. *et al.* Main-chain engineering of polymer photocatalysts with hydrophilic non-conjugated segments for visible-light-driven hydrogen evolution. *Nat Commun* **13**, 5460 (2022).

43. Wang, Y., Meng, H.-M., Song, G., Li, Z. & Zhang, X.-B. Conjugated-Polymer-Based Nanomaterials for Photothermal Therapy. *ACS Appl. Polym. Mater.* **2**, 4258–4272 (2020).

44. Inal, S., Rivnay, J., Suiu, A.-O., Malliaras, G. G. & McCulloch, I. Conjugated Polymers in Bioelectronics. *Accounts Chem Res* **51**, 1368–1376 (2018).

45. Wang, N., Yang, A., Fu, Y., Li, Y. & Yan, F. Functionalized Organic Thin Film Transistors for Biosensing. *Accounts Chem Res* **52**, 277–287 (2019).

46. Guo, K. *et al.* Rapid single-molecule detection of COVID-19 and MERS antigens via nanobody-functionalized organic electrochemical transistors. *Nat Biomed Eng* 1–12 (2021) doi:10.1038/s41551-021-00734-9.

47. Ji, X., Lin, X. & Rivnay, J. Organic electrochemical transistors as on-site signal amplifiers for electrochemical aptamer-based sensing. *Nat. Commun.* **14**, 1665 (2023).

48. Migneault, I., Dartiguenave, C., Bertrand, M. J. & Waldron, K. C. Glutaraldehyde: behavior in aqueous solution, reaction with proteins, and application to enzyme crosslinking. *BioTechniques* **37**, 790–802 (2004).

49. Moggia, G., Kenis, T., Daems, N. & Breugelmans, T. Electrochemical Oxidation of d-Glucose in Alkaline Medium: Impact of Oxidation Potential and Chemical Side Reactions on the Selectivity to d-Gluconic and d-Glucaric Acid. *ChemElectroChem* **7**, 86–95 (2020).

50. Jiang, Y. *et al.* A universal interface for plug-and-play assembly of stretchable devices. *Nature* **614**, 456–462 (2023).

Methods

Materials

All the chemicals in this work were used without further purification. 2-hydroxy-2-methyl-propiophenon, 2,5-bis(trimethylstannyl)thiophene, bromobenzene, deuterium oxide, chloroform, ethyl acetate, hexane, acetone, dimethyl sulfoxide, dimethyl sulfoxide-d_6, poly(vinylidenefluoride-co-hexafluoropropylene), tris(dibenzylideneacetone)dipalladium, tri(o-tolyl)phosphine, sodium chloride, poly(sodium 4-styrenesulfonate) solution (M_w=200 kDa, 30 wt.% in H_2O), trimethyl(phenyl)tin, glucose oxidase (from *Aspergillus niger*, Type X-S), D-(+)-Glucose, choline chloride, acrylamide, ammonium hexafluorophosphate, ferrocene, dextran (M_r ~ 70000), 1-ethyl-3-methylimidazolium bis(trifluoromethylsulfonyl)imide were purchased from Sigma-Aldrich. Acrylic acid was purchased from Alfa Aesar. Tetraethylene glycol dimethylacrylate was purchased from Polysciences Inc. 5,5'-dibromo-3,3'-bis(2-(2-(2-methoxyethoxy)ethoxy)ethoxy)-2,2'-bithiophene was purchased from SunaTech Inc. Styrene-Ethylene-Butylene-Styrene was obtained from Asahi Kasei. Polydimethylsiloxane (Sylgard 184) was purchased from Ellsworth Adhesives. Ecoflex 00-30 was purchased from Smooth-on, Inc. Polyethylene glycol-fluorescein isothiocyanate (M_w = 20 kDa) was purchased from Wuhan Borenpharm Co.

Synthesis of p(g2T-T)

The polymerization of p(g2T-T) was carried out according to the reported method[51], with the Biotage Initiator$^+$ microwave reactor. Briefly speaking, in a clean 5.0 mL microwave vial, 63.8 mg of 2,5-bis(trimethylstannyl)thiophene (155.7 μmol) and 100.0 mg of 5,5'-dibromo-3,3'-bisalkoxy-2,2'-bithiophene (155.7 μmol) were dissolved in 2.0 mL of anhydrous degassed chlorobenzene.

$Pd_2(dba)_3$ (2.48 mg, 2.71 μmol) and $P(o\text{-}tol)_3$ (3.76 mg, 12.3 μmol) were added and the vial was sealed under nitrogen. The vial was subjected to heating: 5 min 100 ℃, 5 min 140 ℃, 5 min 160 ℃, 5 min 180 ℃, 25 min 200 ℃. After polymerization, the vial was cooled, 40 μL of trimethyl(phenyl)tin was added and the contents were subjected to microwave heating: 2 min 100 ℃, 2 min 140 ℃, 2 min 160 ℃, 2 min 180 ℃, 5 min 200 ℃. Finally, 100 μL 2-bromobenzene was added and the reaction was subjected to microwave heating: 2 min 100 ℃, 2 min 140 ℃, 2 min 160 ℃, 2 min 180 ℃, 5 min 200 ℃. Then the reaction mixture was cooled to room temperature and precipitated in methanol. A formed blue solid was filtered by a filtering paper, and Soxhlet extraction was carried out with hexane, ethyl acetate, acetone, and chloroform for 6 h at each step. The polymer dissolved in hot chloroform. Finally, the polymer chloroform solution was concentrated and dried under a high vacuum. A blue solid was obtained with a mass of ~ 80 mg.

Preparation of p(g2T-T) and hydro-SC thin films

To prepare p(g2T-T) thin film, the polymer was dissolved in chloroform with a concentration of 10 mg/ml, the solution was heated under 90 ℃ overnight. The film was obtained by spin-coating the solution onto the substrate. The preparation of hydro-SC thin film was fully carried out within the glovebox except for the solvent exchange step. To prepare the precursor solution of hydro-SC, the p(g2T-T) was dissolved in DMSO with a default concentration of 20 mg/ml unless specified, the solution was heated under 90 ℃ overnight to yield a viscous solution. Then the hydrogel precursors were added to p(g2T-T) solution with the default acrylic acid (AAc) concentration of 200 mg/ml, and tetraethylene glycol dimethylacrylate and 2-hydroxy-2-methyl-propiophenon concentration were kept at 0.5 wt% of AAc unless specified. The precursor solution was mildly heated under 60 ℃ with stirring for 2 min to mix all compounds. Before spin-coating, the precursor solution was cooled to room temperature to minimize the DMSO evaporation during the coating process. The spin coating was accomplished in 5 s to get a uniform liquid layer with minimal evaporation. Then the film was crosslinked under UV light (UV Nail Lamp, 340-380 nm wavelength, 36 W) for 10 min. Afterward, the DMSO-gel film was taken out of the glove box and immersed in DI water for 5 min to accomplish the solvent exchange process.

Cryogenic electron microscopy

The Cryo-EM sample was prepared using Vitrobot. The chamber was preheated to 60 ℃ and then 1 μL of heated 20 mg/ml p(g2T-T) solution was added to the carbon-coated TEM grid, which was immediately immersed in liquid ethane to freeze the solution structure. The samples were imaged by the FEI Talos (S)TEM, operated at 200 kV.

Scanning electron microscopy

The DMSO gel and hydro-SC were prepared using the aforementioned protocol. The hydro-SC was kept in water to ensure sufficient swelling. Both samples were immediately immersed in liquid nitrogen for freezing and further dried under vacuum at 4 ℃ for 7 days. The samples were imaged by the Carl Zeiss Merlin SEM, operated at 3 kV.

Conductive atomic force microscope (C-AFM)

The C-AFM measurement was performed by using the C-AFM mode of Cypher ES Environmental AFM with ASTELEC-01 probe and the dual gain C-AFM probe holder (gain = 1μA/1nA/V). The dried hydro-SC and DMSO gel samples were prepared on a SiO_2 substrate deposited with Au. Magnets were placed separately on Au and sample film and sealed with Ag paste to realize ideal contact. Before measurement, the sample bias was zeroed by applying an offset voltage from the AFM hardware. During the measurement, 1 V bias was applied across samples and the current was converted to a voltage and then amplified and recorded by the AFM hardware.

OECT measurement

OECT was fabricated by preparing polymer thin film on the glass substrate, which is pre-deposited with 5 nm Ti and 100 nm Au via a shadow mask as the D/S electrodes (channel length = 1 mm, channel width = 2 mm). For OECT measurement, poly(dimethylsiloxane) (PDMS) strips prepared with a 15:1 base/crosslinker ratio were placed on both sides of the channel to define the channel area and confine the electrolyte. The aqueous electrolyte (100 mM NaCl solution unless specified) was carefully dropped on the channel. During the test, an Ag/AgCl pellet (Warner instruments, E210), which was equilibrated in the testing electrolyte overnight, was immersed in the electrolyte as the gate electrode. The device measurement was carried out using a Keithley 4200 semiconductor system.

Grazing incidence X-ray diffraction (GIXD) measurement

GIXD measurements were conducted on beamline 7.3.3 at the Advanced Light Source in Berkeley Lawrence National Lab. Data were collected under a helium environment with an incident beam energy of 10 keV and an incidence angle of 0.15°. Thin-film samples were prepared and dried on Si wafers. The scattering signal was collected by a Pilatus 2M detector and processed using Igor 8 software combined with the Nika package and WAXSTools.

Cyclic Voltammetry (CV)

The CV measurements were carried out using the PalmSens electrochemical workstation with the polymer thin film on Au as the working electrode. To prepare the samples, the p(g2T-T) was coated on the Au electrode, and hydro-SC was transferred to the Au electrode using poly(sodium 4-styrenesulfonate) (PSS) as the sacrificial layer. Ag/AgCl was used as the reference electrode and a Pt plate was used as the counter electrode. For measurement in acetonitrile and water, ammonium hexafluorophosphate and NaCl were used to prepare 100 mM supporting electrolyte, respectively. All CV tests were performed with a scan rate of 0.1 V/s.

Operando UV-vis measurement

The Operando UV-vis measurement was carried out by combining the Shimadzu UV-3600 Plus UV-VIS-NIR spectrophotometer with a manually built electrochemical cell controlled by the PalmSens electrochemical workstation. An Ag/AgCl wire, Pt wire, and film-coated indium tin oxide (ITO) glass were used as the reference, counter, and working electrode, respectively. To acquire the UV-vis spectrum of p(g2T-T) and hydro-SC at the non-doped state, a -0.2 V bias was applied to the working electrode before the acquisition. To perform the operando UV-vis measurement, bias was applied within the range of -0.2V and +0.5V with a 0.1V step. The UV-vis spectrum at each bias condition was acquired after the equilibrium.

OECT measurement with an ion exchange gel

The OECT measurement based on the ion exchange gel was modified with the reported method[36]. The precursor solution for ion gel was prepared by dissolving poly(vinylidene fluoride-co-hexafluoropropylene) (PVDF-HFP) and the ionic liquid (1:4, w/w) in acetone with the following proportions: 17.6 wt % 1-ethyl-3-methylimidazolium bis(trifluoromethylsulfonyl)imide, 4.4 wt %

PVDF-HFP, and 78 wt % acetone. To test the OECT performance with an ion gel, about 100 uL of precursor solution was dipped into the channel area. The device was left for 10 min until the acetone was fully evaporated, resulting in the formation of a thin ion gel layer. Then 100 mM aqueous NaCl solution was dropped on the ion gel and an Ag/AgCl pellet was immersed into the aqueous solution as the gate electrode. The device measurement was carried out using a Keithley 4200 semiconductor system.

Mobility measurement based on OECT configuration

Before mobility measurement, the thin film was fully dried and carefully defined as individual channels by using a blade to remove the excess materials under the microscope. The μ of redox-active polymer semiconductors under OECT operation was obtained by measuring the hole transit time (τ_h) as reported[52]. Briefly speaking, different constant gate currents (I_g) have been applied to the device under constant drain bias (V_{ds}). Then the transient slope is plotted versus I_g to calculate the τ_h. The mobility is calculated by:

$$\mu = \frac{L^2}{\tau_h \times V_{\mathrm{ds}}}$$

where the μ, L are the mobility and channel length, respectively.

Floating-on-water tensile test

The floating-on-water tensile test was carried out based on the reported method[37]. Briefly speaking, the PSS sacrificial layer was prepared by coating 6 wt% PSS aqueous solution onto a plasma-treated silicon wafer at 2000 r.p.m. for 1 min. The DMSO gel was prepared on top of the sacrificial layer and dried under vacuum and cut into testing strips. For the tensile test, the test strip was released in 100 mM aqueous NaCl solution to form a hydro-SC, and left for 5 min to reach the swelling equilibrium. Then the linear stage and load cell PDMS clamps were attached to the pads at each end of the hydro-SC film. During the tensile test, each film was elongated at a rate of 0.04 mm/s, while in the meantime the force was measured at a frequency of 10 Hz. Young's modulus was calculated by fitting the strain stress curve within the 0-1% strain range.

OECT performance measurement under strain

Microcracked Au was fabricated by evaporating Au on the SEBS substrate (SEBS 1052) via a shadow mask (channel length = 1 mm, channel width = 2 mm) at a rate of 0.2 Å/s with the substrate heated at 60 °C[50]. The hydro-SC thin film was transferred to the SEBS with PSS as the sacrificial layer. The hydro-SC film was then dried and gently baked under 60 °C to improve the adhesion. For the OECT test, 100 mM aqueous NaCl solution was dropped onto the hydro-SC, and the device was stretched to the targeted strain using a stretcher for electrical measurement.

Conformability test

The tendon replica was fabricated by molding a beef tendon twice with EcoFlex. The DMSO gel and p(g2T-T) films were prepared on the PSS sacrificial layer. Both films were released in 100 mM aqueous NaCl solution and picked up with a PET tape as a rigid frame. Then the hydro-SC and p(g2T-T) films were carefully laminated onto the tendon replica and imaged under the Olympus OLS5000 LEXT 3D microscope.

Preparation of PAAc and PAAm hydrogel

To prepare PAAc or PAAm hydrogel as the implant or substrate, 250 mg/ml monomers (AAc or AAm), 5 mg/ml tetraethylene glycol dimethylacrylate, 2.5 mg/ml 2-hydroxy-2-methyl-propiophenon were mixed in deionized water and purged with N_2 for 15 min. The mixture was then injected into a rubber cell sandwiched by two glass substrates and crosslinked under UV light (UV Nail Lamp, 340- 380 nm wavelength, 36 W) for 10 min to yield the hydrogel.

Animal implantation surgeries

6- to 8-week-old male C57BL/6 mice were purchased from Jackson Laboratories. Preoperatively, all mice received subcutaneous injections of 5 mg/kg of Meloxicam for pre-surgery analgesia. All mice were anesthetized using 3% isoflurane in oxygen, and the backs of all mice were shaved. All mice received eye lubricants to prevent dehydration-induced blindness. Then, the shaved backs of all mice were sterilized by scrubbing with betadine and alcohol pads in an alternating fashion, repeated two times. Two transverse incisions, 1 cm in length, were made in the upper and lower backs. The blade tip of a pair of scissors was inserted into the subcutaneous space through the incisions, and two subcutaneous pockets, flanking each incision, were made via blunt tissue dissection using the blunt sides of a pair of scissors. Two implants (5 mm in diameter and 1 mm in

thickness) were inserted in the subcutaneous pockets on both sides of each incision, towards the limbs of the mice, for a total of four implants per mouse. Following surgery, all mice were given subcutaneous injections of 5 mg/kg of Meloxicam once every 24 hours for two days. Wound clips were removed after 10 days.

Histological processing for H&E and Masson's trichrome staining

After 4 weeks post-implantation, all mice were euthanized by CO_2 asphyxiation, followed by cervical dislocation. Afterward, the backs of all the mice were shaved. The implants and the surrounding tissues were explanted and fixed in 10% neutral buffered formalin for 24 h. After fixation, the implants and tissues were transferred to 70% ethanol for 24 hrs. The materials were then paraffin-embedded, sectioned (5 μm), and stained for H&E using standard procedures by the Human Tissue Resource Center at the University of Chicago. Masson's trichrome staining was carried out in-house using standard procedures. Whole-section scans of H&E and MTS-stained tissue sections were conducted using the Olympus VS200 Slideview Slide Scanner.

Patch-clamp local photocurrent measurement

Photocurrent measurements was carried out using previously reported methods[17]. The patch-clamp set-up integrated with an upright microscope (Olympus, BX61WI) with a ×20/0.5 numerical aperture water-immersion objective was used for photocurrent measurements. Light pulses were delivered using episcopic illumination with a dichroic mirror (for 625 nm LEDs, FF660-Di02-25×36, Semrock). Clamp voltage and current were measured using silver chloride electrodes and amplified using an AxoPatch 200B amplifier (Molecular Devices). Voltage-clamp levels and light pulsing were digitally controlled using TTL or analogue signals delivered from a Digidata 1550 digitizer (Molecular Devices) controlled with Clampex software (Molecular Devices). Glass pipettes were pulled in a P-97 micropipette puller (Sutter Instrument), usually to a resistance of 2 MΩ and filled with ×1 PBS. During the measurement, the semiconductor was placed in a petri dish filled with ×1 PBS and positioned in the center of view. The pipette tip was lowered close to the surface of the material (<10 μm), and the measurement sequence was executed. The sequence lasted 400 ms, with an initial voltage level of −0.5 mV between 100 and 300 ms. At 200 ms, a light pulse (1 ms, 5 ms, 10 ms, 20 ms, or 50 ms) was administered to provoke a photoresponse from the

material. The holding current was adjusted so that the current in the first voltage level was close to 0 pA (usually under 2,000 pA).

Thermal imaging for photothermal effect study

The hydro-SC and p(g2T-T) films were prepared on a PSS sacrificial layer and peeled off by a PDMS stamp. Both films were dried and heated under 635 nm laser (Laserglow) with a 5 mm diameter spot. The spatial distribution of temperature was measured by the thermal camera (Hikmicro). For heating on skin tissue, a piece of the hydro-SC film was laminated to a piece of wet pig skin with the other side encapsulated by PDMS. The heating and recording were performed in the similar way with a radiation power of 318 mW/cm^2, the recording was performed by a Optris PI 640i thermal camera.

Diffusion test

Both p(g2T-T) and hydro-SC films were prepared on the polytetrafluoroethylene substrate and peeled off using adhesive PET tape as the rigid frame. The peeled films were carefully sandwiched between two glass tubes and sealed with epoxy resin. Polyethylene glycol-fluorescein isothiocyanate (PEG-FITC) solution (50 μM in PBS buffer) and PBS buffer were injected on two sides of the tube. The tubes were left horizontally for 24 hrs. The images were taken under UV light. The fluorescent spectrum was measured by the HORIBA Fluorolog-3 Spectrofluorometer.

GOx immobilization and glucose sensing

Hydro-SC was prepared with the p(g2T-T) concentration of 20 mg/ml and AAm concentration of 300 mg/ml, tetraethylene glycol dimethylacrylate concentration of 3 mg/ml, and 2-hydroxy-2-methyl-propiophenon concentration of 3 mg/ml. Hydro-SC or p(g2T-T)-based OECT device was fabricated (channel length = 0.2 mm, channel width = 4 mm) with an in-plane Au as the gate electrode. The device channel was then incubated in PBS buffer containing 10 mg/ml GOx and 5 mg/ml glutaraldehyde for 24 hrs at room temperature. After functionalization, the device was rinsed with PBS buffer 3 times, dried by nitrogen blow, and then carefully isolated as individual channels using a blade under the microscope. For glucose sensing, the glucose solutions were prepared with PBS buffer and carefully added to the channel. Following the addition of glucose,

the device was incubated for 10 min and then the transfer curve was acquired from +0.4 V to -0.4 V with a scan speed of 40 mV/s.

X-ray photoelectron spectroscopy (XPS)

All testing samples were prepared on Si substrate. Both N1s and C1s spectrum of GOx-modified films were acquired using XPS. The depth-profiling XPS was done with Kratos AXIS Nova with a monochromatic Al Kα X-ray source and a delay line detector system with Ar1000+ with 10 keV to etch until the Si element was detected.

Methods References

51. Nielsen, C. B. *et al.* Molecular Design of Semiconducting Polymers for High-Performance Organic Electrochemical Transistors. *J Am Chem Soc* **138**, 10252–10259 (2016).

52. Bernards, D. & Malliaras, G. Steady-State and Transient Behavior of Organic Electrochemical Transistors. *Advanced Functional Materials* **17**, 3538–3544 (2007).

Data availability

All source data are provided within this paper and supplementary information. All relevant data are available from the corresponding author on reasonable request.

Acknowledgments

We thank the University of Chicago Animal Resources Center (RRID: SCR_021806) for animal housing and use of their facility and equipment. All the animal experiments performed in this research were approved by the Institutional Animal Care and Use Committee of the University of Chicago under the protocol ACUP 72702. This work used the Soft Matter Characterization Facility (SMCF) and the Materials Research Science and Engineering Center (MRSEC) at the University of Chicago. This research used beamline 7.3.3 of the Advanced Light Source, which is a DOE Office of Science User Facility under contract no. DE-AC02-05CH11231. Y.W. was supported in part by an ALS Doctoral Fellowship in Residence.

Author Contributions

S.Wang conceived of and supervised this work. Y.D. and S.Wang designed the experiments. Y.D. synthesized the polymers and hydro-SCs. N.L. and N.S. performed and analyzed NMR. Y.D., Y.Li, S.Li and S.C. fabricated and tested the OECT. Y.D. and Youdi Liu performed the conformability test. S.Wai performed biocompatibility study. Yuzi Liu, J.X. and C.F. performed and analyzed the cryo-EM results. Y.Li performed SEM imaging. Y.D. and C.F. performed the liquid AFM for swelling ratio measurement. Y.W. and C.Z. performed the GIXD characterizations. Z.C., Y.W., and X.G. performed the FOW measurements. W.L. measured the fluorescent spectroscopy. P.L., J.S., S.Lee and B.T. performed the measurements for studying the photoelectrochemical and photothermal effect. Y.D. and M.W. did the thickness measurement. Y.D. and N.S. performed the diffusion test on semiconductor. Y.D., N.S. and N.L. did the enzyme immobilization and sensing test. C.Z. and S.S. helped analyze the results. Y.D. and S.Wang wrote the paper. All authors reviewed and commented on the manuscript.

Competing interests

The authors declare no competing interests.

Additional information

Supplementary information The online version contains supplementary material available at ***

Correspondence and requests for materials should be addressed to Sihong Wang.

Peer review information